Measurements of current sheet canting in a pulsed electromagnetic accelerator

T. E. Markusic, E. Y. Choueiri, and J. W. Berkery
Electric Propulsion and Plasma Dynamics Laboratory (EPPDyL), Mechanical and Aerospace Engineering Department, Princeton University, Princeton, New Jersey 08544

(Received 5 November 2003; accepted 19 April 2004; published online 28 September 2004)

The phenomenon of current sheet canting in pulsed electromagnetic accelerators is the departure of the plasma sheet (that carries the current) from a plane that is perpendicular to the electrodes to one that is skewed or tipped. Developing an understanding of current sheet canting is important because it can detract from the propellant sweeping capabilities of current sheets and, hence, negatively impact the overall efficiency. In the present study, photographic, magnetic, and laser-interferometric diagnostics were implemented to study current sheets in an experimental pulsed electromagnetic accelerator, using a variety of propellants and pressure levels. The interferometric measurements were used to quantify the canting angle during the stable phase of propagation. The canting angle was found to increase with the atomic mass of the propellant and the current sheet was always found to tilt such that the anode current attachment leads the cathode attachment. © *2004 American Institute of Physics*. [DOI: 10.1063/1.1779631]

I. INTRODUCTION

Pulsed electromagnetic accelerators are devices which use intense bursts of electrical current $[O(10^4-10^6)\ \mathrm{A}]$ to create high speed $[O(10^3-10^5)\ \mathrm{m/s}]$ jets of plasma. They find application as plasma sources in many basic plasma science experiments (see, for example, Ref. 1) as well as in a specific genre of electric space propulsion device called the pulsed plasma thruster (PPT) as described in Ref. 2. The present work is motivated by the desire to improve the performance of pulsed electromagnetic accelerators in the context of plasma propulsion.

PPTs have the potential for fulfilling the attitude control requirements on a satellite at greatly reduced mass and cost. They are also being considered for constellation maintenance for missions such as interferometric imaging of the Earth from space, or deep space, from an Earth orbit (see, for example, Ref. 3). The benefits of PPTs are their simplicity, very small impulse bits for precise control of satellite motion, reliability, and high specific impulse. Two classifications of PPTs exist, corresponding to the form of propellant used: gas-fed (GFPPT) or ablative (APPT) propellant. The gas-fed variety has the advantages of a "clean" exhaust plume and high specific impulse. The ablative version of the PPT uses a solid propellant, such as Teflon, to provide other advantages such as compactness and overall ease of system integration; however, plume contamination (mostly from carbon soot) and lower specific impulse may limit the application of APPTs for some missions.

The present work focuses on understanding the spatial configuration of the current sheet in an experimental accelerator (the accelerator used was of the *gas-fed* variety, where electromagnetic acceleration is the dominant mode of acceleration; the results of this study may not be directly relevant to the *ablative* thrusters, where electrothermal acceleration may be significant). More specifically, we present experimental measurements which quantify the degree to which current sheets tilt (or cant), relative to the electrodes, as they propagate. The degree of canting was measured using a variety of techniques and under a variety of experimental conditions.

II. REVIEW OF THE PROBLEM

A. Definition of the problem

The phenomenon of current sheet canting is the departure of the current sheet from perpendicular attachment to the electrodes to a skewed, or tipped, attachment. Ideally, we would like the current sheet to initiate at the breech of an accelerator, perpendicular to the electrodes, and remain so as it propagates axially. In contrast, as time progresses, current sheets are observed to severely tilt, or cant, as they propagate.

While direct measurements of the impact of canting on overall thruster performance remain to be carried out, we can make arguments which suggest that it will have adverse implications. Canting creates off-axis components of thrust, which constitute a profile loss. Considering the work done by the current sheet, it is clear that a canted current sheet will apply a force to the propellant transverse to the thrust axis and thus expend energy, which is not converted into useful thrust. Canting may also undermine the effective sweeping up of propellant as the current sheet propagates. The effect of canting may be to force the plasma entrained by the current sheet towards one of the electrodes, where it stagnates and is then left behind. Indeed, canted current sheets may act, undesirably, like *real* snowplows—never accumulating but, rather, throwing their load to the side as they pass by.

B. Review of past research

Review of the work of earlier researchers reveals that our understanding of the acceleration mechanism in PPTs is deficient in several areas—canting being one of them. We

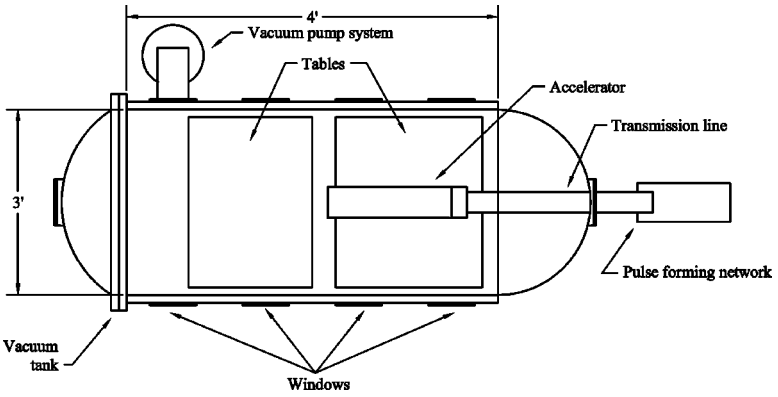

FIG. 1. Top-view schematic of the general experimental layout.

are, by no means, the first group to observe current sheet canting. The literature from the early GFPPT researchers (see, for example, Refs. 4–12) indicates that the phenomenon was ubiquitous—occurring in a variety of different electrode geometries and experimental conditions. However, detailed treatment of the subject is limited with most references to the phenomenon being anecdotal in nature. A review of the earlier studies has presented by Markusic (as given in Ref. 13); the conclusions of that review can be summarized as follows.

(1) Current sheet canting always occurs in an orientation such that the anode current attachment leads the cathode current attachment.

(2) Current sheets are always observed to cant with nitrogen and argon propellant—irrespective of geometry (rectangular, coaxial, *z* pinch, inverse *z* pinch, and parallel rod), gas pressure, or current level.

(3) Uncanted hydrogen and deuterium current sheets have been observed but only with specially prepared electrodes.

(4) Ion current conduction is suspected to play an important role in establishing the overall current pattern.

(5) Current sheets appear to exhibit invariant features (e.g., anode foot, cathode hook, and canting) over a wide range of geometries, propellent species, and gas pressure and current levels.

The conclusions enumerated above show that current sheet canting has been observed in many studies. However, there was no unanimity of opinion as to its origin. Furthermore, no study has accurately quantified canting angles and their dependencies. The present study attempted to address these deficiencies through dedicated experiments.

III. APPARATUS

An experimental apparatus was constructed to investigate current sheet canting; the experiment was called the current sheet canting experiment (CSCX). To isolate the canting effect we have followed the lead of Lovberg (as described in Ref. 11) in using a rectangular geometry accelerator. This geometry eliminates the radial field variation found in the coaxial geometry, provides ease of diagnostic access, and is amenable to analytical studies. One significant difference in our study was the use of a pulse forming network; almost all of the experimental results described in earlier studies used sinusoidal wave forms. In doing so, our intent was to eliminate any phenomena that result from current transients, and to make analytical studies more tractable.

A. General experimental layout

The basic components of the CSCX experimental apparatus (illustrated in Fig. 1) are the accelerator, pulse forming network, vacuum facility, and data acquisition equipment. Tables inside the vacuum chamber support the accelerator and provide mounting surfaces for optics and diagnostic probes. A 4 ft.$\times$6 ft. optics table, positioned next to the tank, was used to lay out optical diagnostics. Glass windows on the sides of the vacuum chamber provided optical access to the accelerator discharge. Two Faraday cages were used to house the data acquisition equipment.

B. Accelerator

The CSCX accelerator is a parallel-plate pulsed plasma accelerator with glass sidewalls (a schematic illustration with relevant dimensions is shown in Fig. 2). The dimensions of the discharge chamber were chosen to be similar to those found to "work" by earlier researchers (see, for example, Ref. 14). The electrodes are made of copper and the sidewalls are made of Pyrex. The sidewalls reduce the region accessible to the discharge to 10 cm (width), whereas the electrodes themselves are 15 cm wide. The motivation for using Pyrex sidewalls is several-fold: they provide an excellent optical view of the discharge, they isolate the current sheet to a well-defined spatial region, they isolate the discharge from electric field singularities near the edges of the electrodes, and they isolate the discharge from the rapidly fringing magnetic field at the edges of the electrodes. The two latter benefits tend to make the discharge environment more conducive to the formation of current sheets that are spatially uniform transverse to the direction of propagation.

Propellant loading was accomplished using the ambient fill technique. After the vacuum tank was pumped down to its base pressure, the entire tank was brought up to the desired operating pressure with the chosen propellant. Three different initial gas pressure levels (75, 200, and 400 mTorr) and eight different propellants (hydrogen, deuterium, helium, neon, argon, krypton, xenon, and methane) were tested. The ambient loading technique resulted in a uniform gas distribution within the accelerator prior to discharge initiation.

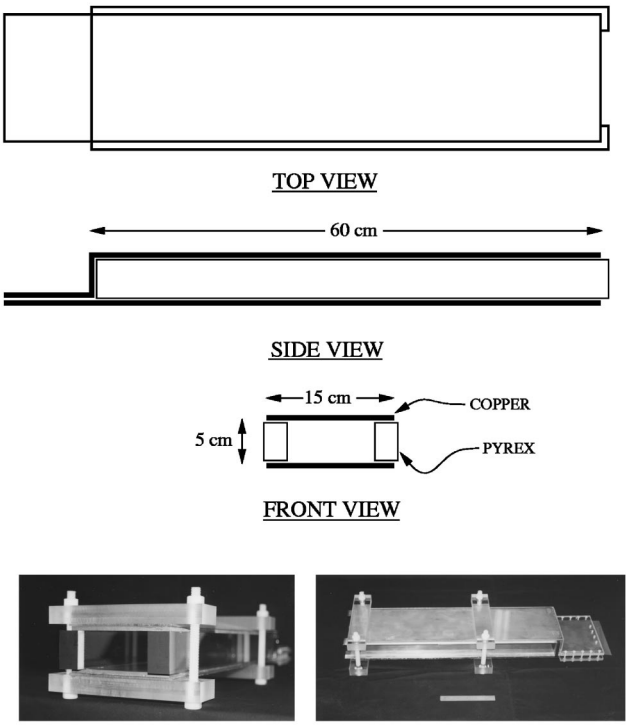

FIG. 2. Schematic and photographs of the CSCX accelerator.

Approximately ten pulses at full capacitor bank voltage were executed before taking data in an attempt to remove adsorbed gases from the electrodes.

The accelerator is powered by a ten-stage pulse forming network (PFN). The values of the electrical components at each stage were chosen to give a nearly flat current profile with a pulse width that roughly corresponds to the time it takes the current sheet to traverse the length of the accelerator. Each stage is composed of a 10 μF capacitor in series with a 100 nH inductor. The maximum bank voltage was 10 kV, yielding a total discharge energy of 5 kJ. The PFN was switched into the accelerator using an ignitron. The peak current was $\approx$80 kA with an initial rise rate on the order of 10^{11} A/s. The duration of each (flat-top) pulse was about 25 μs, followed by several cycles of damped ringing. Data was only acquired during the first-half cycle where, after the submicrosecond starting transient, the current was steady.

In general, the accelerator performed very well; current sheets were generated in the expected manner (i.e., formation at the breech and propagation to the exit) and the experiments were very repeatable. High speed photographs (see Sec. V B) taken of different discharges (with the same initial conditions and same camera time delay) were practically indistinguishable.

C. Vacuum facility

The vacuum facility used in this experiment (see Fig. 1) is described in detail in Ref. 15. The vacuum vessel is a 3 ft. diameter, 6 ft. long cylindrical tank made entirely of Plexiglass (which has been shown to eliminate the electromagnetic interactions sometimes found in metallic vessels) with glass optical access windows. Gases were introduced into the tank using a regulated feed through. The tank uses a diffusion pump with a freon-cooled trap to achieve a base pressure of 1×10^{-5} Torr. SubmilliTorr pressures were measured with a CVC cold cathode gauge. All pressures above 1 mTorr were monitored using a MKS Baratron vacuum gauge; this gauge gave a gas-species-independent reading, which allowed an accurate measurement of the initial propellant pressure in the accelerator.

IV. DIAGNOSTICS

High speed photography, schlieren photography, laser interferometry, magnetic field probing, and emission spectroscopy were used to diagnose current sheets in the CSCX apparatus. Here we briefly describe the photographic, magnetic, and interferometric diagnostics. Descriptions of the other diagnostics, implementation details, and calibration procedures are given in Ref. 13.

A. High-speed photography

A Hadland Photonics Imacon 792LC camera was used to obtain series of photographs that show the spatial evolution of the current sheet during a current pulse. The camera is capable of taking pictures at a rate of up to 20 MHz and provides up to 16 images printed on Polaroid film. In the experiments presented here, the framing rate was set to 500 kHz; the exposure time for each image was 400 ns. The side of the accelerator was imaged through a chamber window (see Fig. 1). In order to more easily visualize the spatial position of the current sheets and to estimate the size and orientation of current sheet features, a black screen with white gridding (1 cm spacing) was placed on the opposite side of the accelerator.

B. Magnetic field probes

Magnetic field probes were used to map the spatial and temporal evolution of the magnetic field throughout the entire discharge chamber. The probes used were magnetic induction coils, commonly referred to as *B*-dot probes. These probes are simply linear coils of wire that generate an emf proportional to the time variation of the magnetic flux through the coil. The 2.5 mm diameter coils are attached to the two inner conductors of triaxial cables; the cable and coil-cable assemblies are encased by 6 mm diameter, 60 cm long quartz tubes. The probe voltage was measured directly and integrated numerically to determine $B(t)$. The probes were mounted on an electrically actuated translation stage, which allowed their position to be continuously adjusted from the breech to the exhaust.

C. Laser interferometry

A two-chord heterodyne laser interferometer with electronic quadrature phase detection was constructed. The system functionally consists of two interferometers in the Mach-Zehnder configuration. This type of interferometer detects phase differences between the "scene" and "reference" beams. When these two beams are recombined at the detec-

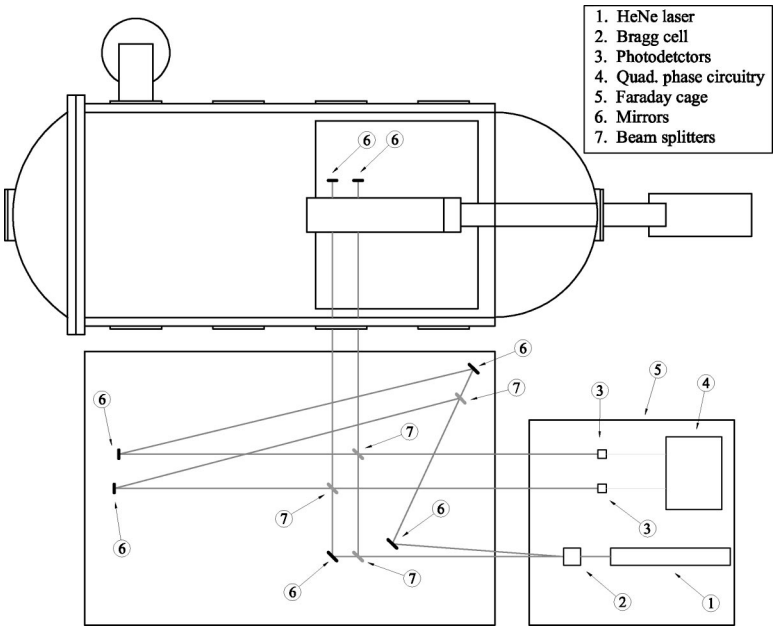

FIG. 3. Schematic of laser interferometry layout for current sheet speed determination (configuration 1).

tor, any phase mismatches between the beams causes amplitude variations in the detector output due to constructive or destructive interference.

A schematic of the experimental layout is shown in Fig. 3. The interferometer was used to determine the current sheet speed and canting angle by monitoring the phase variations of two laser beams at different spatial locations within the accelerator; the spatial configuration of the current sheet was inferred through a time-of-flight analysis. The response from two horizontally separated beams ($\approx$10 cm axial separation) were used to determine the propagation speed (the orientation of the optics for this experiment is illustrated in Fig. 3). The beams were retroreflected back through the plasma to give twice the phase shift of a single pass. For canting angle determination, the two beams were positioned at the same axial location, but vertically separated by about 3.5 cm. Additionally, quantitative measurements of the current sheet electron density were obtained from the measured phase shift in each beam.

The specific components used in the interferometer were as follows. The light source was a Coherent model 31-2108 17 mW HeNe laser. The beam splitting into the scene and reference beams, along with modulation of the reference beam, was accomplished using an IntraAction model AOM-405 acousto-optic cell driven by a 40 MHz, 5 W rf power source. Two Thor Labs model PDA155 photo detectors were used. These amplified (1×10^4 V/A) Si detectors have a 50 MHz bandwidth. It was found that, because of the large amount of electromagnetic noise created by the firing of the accelerator, all electronics including the laser, had to be housed in a Faraday cage. Standard optical components (aluminized mirrors, dielectric beam splitters, and antireflection windows) were used to steer the laser beams.

V. EXPERIMENTAL RESULTS

The results from the measurements provide spatially resolved information that expose the evolving current channel structure that leads to a canted current sheet. Below we divide the presentation of the data into three sections; the first section describes the characteristic plasma parameters of the current sheet plasmas, the second section shows general spatial evolution of the current sheet, and the last section summarizes the canting angle measurements for the stable phase of propagation.

A. Characteristic plasma parameters

Figure 4 shows some calculated fundamental quantities, which characterize CSCX current sheet plasmas. These plots were constructed using measured values of magnetic field, electron density, and electron temperature ($p=200$ mTorr data was used in all of the calculations). These values represent the peak measured values as the current sheet propagated through the measurement region near the center of the accelerator. The (spectroscopically acquired) temperature measurement from argon current sheets ($T_e=2.4\pm0.2$ eV) was used in all calculations (as described in Ref. 13). The measured temperature is typical for arc discharges at CSCX pressure and current levels, and no major deviations from the measured temperature are expected amongst the other tested propellants (see, for example, Refs. 12 and 16). The parameters were calculated using their standard definitions (as given in Ref. 17). Some additional characteristic parameter values are tabulated in Table I. Throughout the calculations it was assumed that: $n_i=n_e$, $T_i=T_e$, and $Z=1$.

Let us consider first some characteristic lengths in the CSCX current sheet plasmas. Figure 4(a) shows that the electron and ion gyroradii are small relative to the device dimensions ($\sim$5 cm), which shows that particle orbital motion is, for the most part, not interrupted by the proximity of the electrodes. This figure also shows that the mean free path (Coulomb collisions) is small as compared to the current sheet dimensions ($\sim$1 cm) implying that the plasma is collisional for both electrons and ions. Using the approximate dimensions of the current sheet (1 cm$\times$10 cm$\times$5 cm) and

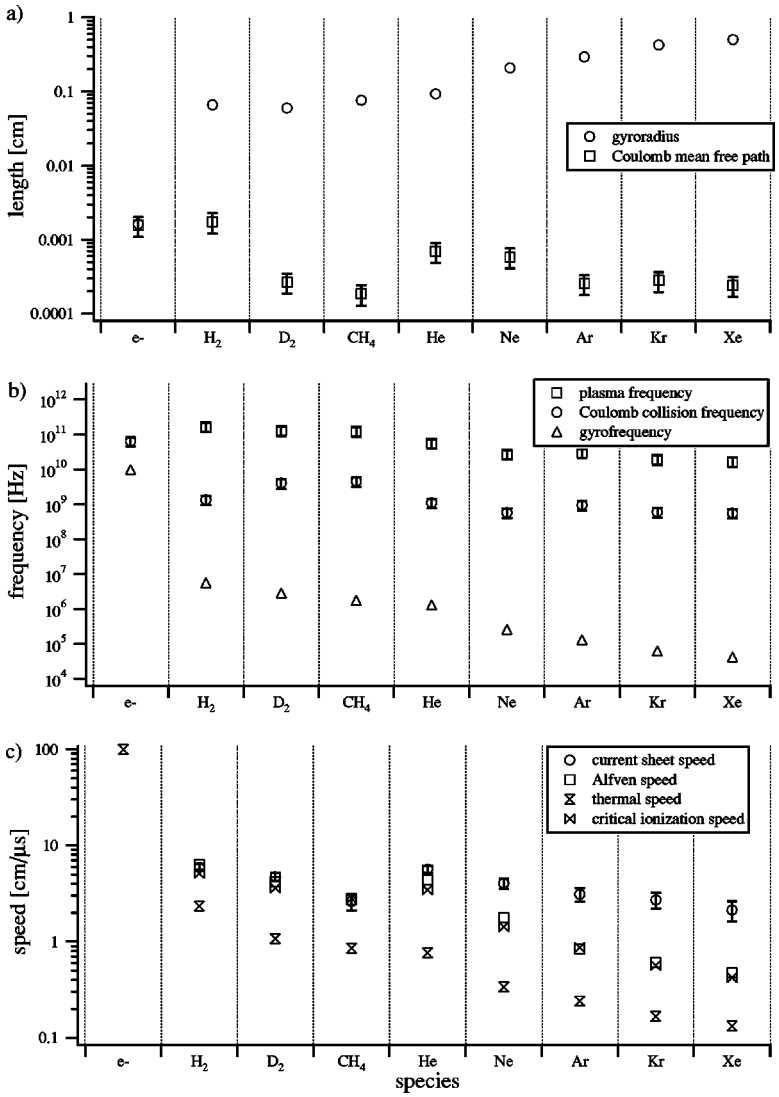

FIG. 4. Characteristics values of (a) length, (b) frequency, and (c) speed in CSCX current sheets (the error bars that are not shown are comparable to the marker size).

the calculated value of the transverse Spitzer resistivity ($\eta_\perp$), the Ohmic resistance of the current sheet is estimated to be 5 mΩ, which is the same order of magnitude as the measured values of 1–5 mΩ (as described in Ref. 13). For the ions, the mean free paths are also seen to be much smaller than the corresponding gyroradii, whereas the electron mean free path and electron gyroradius are seen to be comparable in magnitude. Table I lists two other characteristic lengths: the Debye length (λ_D) and the electron skin depth (δ_e). The debye length is seen to be small compared to the device dimensions, so non-quasineutral electrode sheaths are expected to be small. The small value of the skin depth implies that the plasma is well suited for containing magnetic fields via surface currents, that is, forming current sheets.

TABLE I. Order of magnitude estimates of characteristic parameter values for CSCX current sheets (representative values used: $T=2.4$ eV, $n=3\times10^{16}$ cm^{-3}, $B=0.35$ T).

Parameter	Value
λ_D (cm)	1×10^{-5}
β	1×10^{-1}
δ_e (cm)	1×10^{-3}
Ω_e	1×10^{-1}
$\eta_\perp$ (Ω cm)	1×10^{-2}
Ω_i	1×10^{-3}

Figure 4(b) shows some calculated characteristics frequencies in the CSCX plasmas. Of particular interest is the ratio of the gyrofrequency to the collision frequency—the so-called Hall parameter. Table I shows that the Hall parameter is expected to be small for both electrons (Ω_e) and ions (Ω_i). This implies that minimal Hall effect induced transverse (i.e., perpendicular to both the magnetic field and the applied electric field) components of current are expected to arise. It should be emphasized that these statements only apply to the Hall parameter calculated using the average measured current sheet properties near the midsection of the accelerator—where the canting angle has stabilized. Also, as shown in a subsequent section, the electron density (and hence the Hall parameter) varies greatly at different spatial locations in the current sheet. The electron density was always found to be considerably lower along the anode than elsewhere in the current sheet, implying a considerably

higher Hall parameter near the anode. The Hall effect may play a very important role, as we discuss in Sec. VI, in causing the current sheet to cant, during the early stages of the discharge. Other characteristic parameters listed in Table I are: Debye length (λ_D), electron skin depth (δ_e), transverse Spitzer resistivity ($\eta_\perp$), and plasma beta (β).

Figure 4(c) shows some characteristics speeds in the CSCX plasmas. The measured current sheet speed is seen to track close to the Alfvén (v_A) and critical ionization (v_{ci}) speeds for the lower atomic mass propellants, but diverges at higher atomic mass. This divergence may, in part, be due to the fact that $Z=1$ was assumed in the calculations, whereas higher levels of ionization may have existed in the heavier propellants; this would lead to a lower calculated Alfvén speed, since n_i would actually be lower than n_e (which was measured and used in the calculations) in the plasma. However, even if $Z=2$ is used in the calculation, multiplying the plotted Alfvén speeds by the corresponding factor of $\sqrt{2}$ would be insufficient to bring the Alfvén speeds for the heavier propellants into parity with the measured values. It should also be noted that the plotted Alfvén speeds were calculated using the plasma and field measurements at the *upstream* probe location, whereas the sheet speed measurements were inferred from a time of flight analysis between the upstream *and* downstream locations and, hence, do not represent precisely the same spatial location. Since, as is shown in the following section, the current sheet is seen to accelerate as it propagates, the measured current sheet speed would be expected to be somewhat higher than the predicted, upstream value. The picture is further muddied by the fact (as shown in the next section) that the plasma density appears to decrease (opposite of what is expected) as the current sheet propagates. In summary, there are many factors that could explain the relatively small discrepancy between the Alfvén and measured speeds, primarily the limited resolution of the plasma density measurement, so to discuss it further would take us too far afield from the primary motivation of this paper, which is to quantify the extent of current sheet canting.

B. Evolution of the current sheet discharge

In this section we present photographic, magnetic field, and interferometric data that show how the current sheet evolves in the CSSX accelerator.

1. High-speed photography

High-speed photography was used to obtain multiple images of a propagating current sheet during single discharge event; the interframe delay of the camera was set to 2 μs with 400 ns exposure. When the camera trigger was offset from the initiation of the discharge by 1 μs, the good reproducibility of the discharge structure allowed two separate runs to be interleaved to give a succession of images that show the complete discharge event in 1 μs intervals.

Figures 5 and 6 show photographs of argon discharges at several successive times during the current pulse. The first figure shows the entire discharge chamber; the second is a closeup of the breech region of the accelerator. The Polaroid images were scanned into a computer and processed with photoediting software. Lines were drawn to indicate the position of the electrodes. The two vertical rectangles on the electrodes represent bolts that are used to hold the accelerator together (they caused an optical obstruction between the plasma and the camera). A narrow-pass line filter [488 nm, 10 nm full width at half maximum (FWHM)] was used to

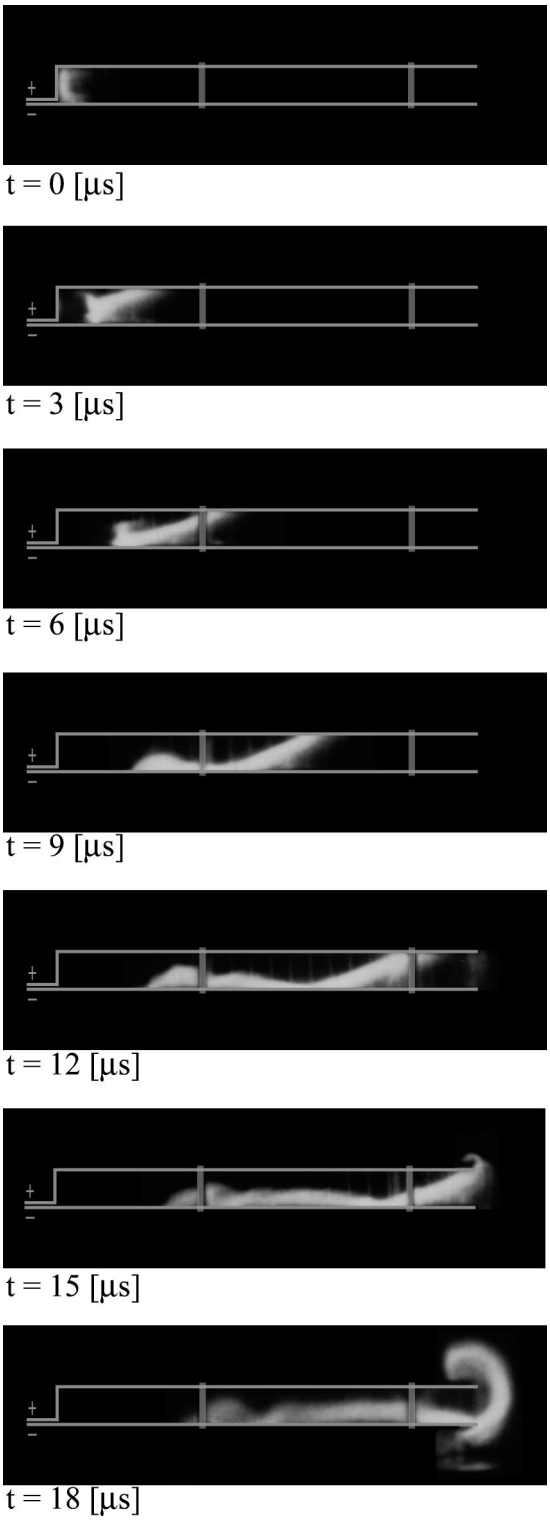

FIG. 5. Series of photographs showing the evolution of the discharge [p = 100 mTorr (argon)].

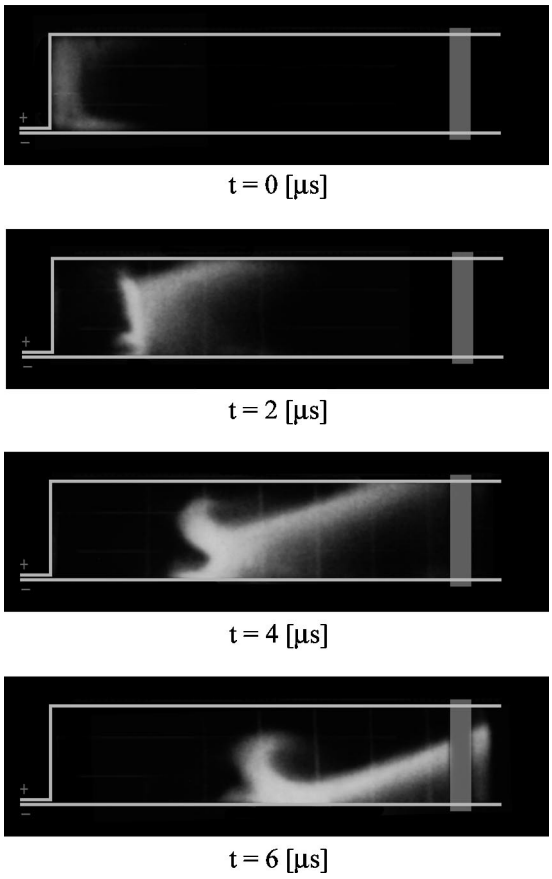

FIG. 6. Series of photographs showing the evolution of the discharge near the breach [$p=100$ mTorr (argon)].

allow only the light emitted by argon ions to enter the camera, to exclude the more spatially diffuse glow of the neutrals, and enhance the contrast in the regions where current was flowing.

The photographs show that the discharge forms at the breech, accelerates down the electrodes, and is ejected from the exit. Immediately after the current sheet moves away from the breech it begins to tilt—with the anode attachment leading that of the cathode. The sheet then stabilizes to a fairly fixed angle, leaving a trail of plasma along the cathode in its wake. Since the anode arc attachment reaches the end of the accelerator first, the ejection of the plasma is quite asymmetric; the current sheet is forced to curl back on itself to reattach at the anode. The discharge propagates 60 cm in ≈ 15 μs implying an average sheet speed of about 40 km/s.

Figure 6 more clearly shows the transition of the arc from its planar initial state, to the fully canted current sheet. As the current sheet leaves the back of the accelerator, it immediately begins to bifurcate. The initial anode attachment point recedes from the electrode, and a diagonal sheet forms. Within several microseconds the sheet attains the canted structure that it maintains for the remainder of its propagation. The base of the arc (cathode attachment) forms a hook-like structure, which has been previously reported in earlier studies (see, for example, Ref. 12).

2. Magnetic field mapping

Magnetic field measurements complement the photographic survey, as the latter indicates the location of the plasma but not necessarily current, whereas magnetic field data provides an unambiguous picture of the current location, but does not directly yield the location of the plasma.

Two magnetic field probes were used to map the evolution of the magnetic field. Time resolved measurements were made over a grid spanning the entire interelectrode space, using a motorized translation stage. This array of points consisted of 72 (axial) $\times$ 6 (transverse) locations. It is important to emphasize that since only two probes were employed, data was obtained at just two out of 432 grid points, during a single discharge.

The magnetic field data was used to construct current density contours, as illustrated in Fig. 7. Features similar to those observed in the photographic study are evident. Immediately after initiation the current sheet is seen to bifurcate near the anode; the leading current channel accelerates ahead of the cathode arc attachment. The trailing anode attachment gradually detaches and a single canted current sheet propagates axially along the remaining extent of the accelerator channel.

It is instructive to consider the differences between the evolution of the magnetic field near the anode versus near the cathode. Figure 8 shows magnetic field data obtained at several different axial locations, with the probes located ≈ 5 mm from each electrode. Each waveform is the record from a single shot. These data provide some insight into the sequence of events, which cause the current sheet to cant during the early stages of the discharge. The plots show very different behavior for the anode current conduction as compared to the cathode attachment. The $x=0.5$ cm curves look very similar; however, a double-peaked structure is evident in the $x=2.5$ cm anode wave form, which is not present in the corresponding cathode trace. The two peaks in the anode data imply the presence of two current conduction paths—bifurcation of the initial current sheet. In the $x=4.5$ cm data the bifurcation is seen to be more pronounced. As the current sheet continues to propagate, the two current attachments spread apart and the leading sheet becomes the dominant current conduction channel (as illustrated by the $x=13.5$ cm data). By the time the current sheet reaches the 21.5 cm location the trailing (initial) current sheet is seen to have disappeared altogether, and the discharge returns to a single current conduction channel mode of operation. The important point here is that no comparable (bifurcation) features are present in the cathode magnetic field wave forms, implying that current sheet bifurcation along the anode is associated with canting.

Figure 9 provides data that reveal the evolution of the magnetic field (and hence the current sheet) for the remainder of the discharge pulse. Figure 9(a) shows the measured current sheet arrival time at 40 different axial locations for both the anode and cathode probes. Each datum point represents the average of four shots. Polynomial curve fits (fifth order) to the data are also shown. By taking the average of the anode and cathode curves, the trajectory of the geometric

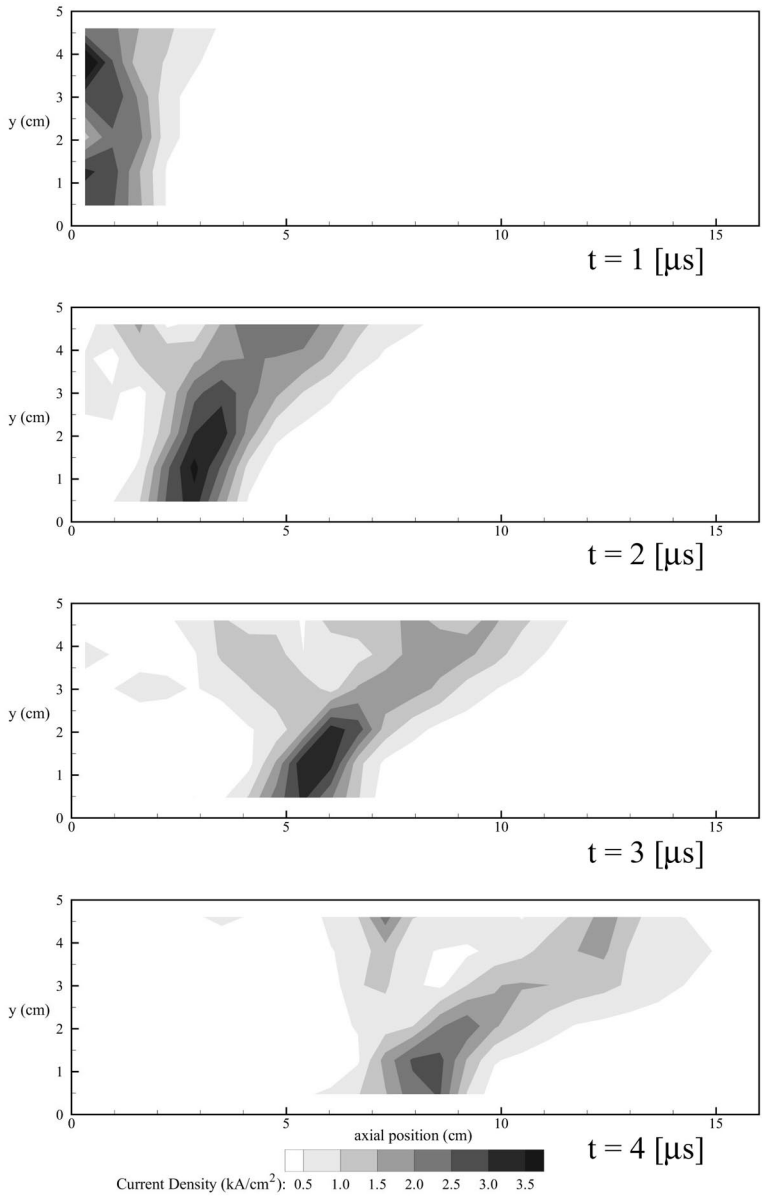

FIG. 7. Current density contours [$p=100$ mTorr (argon)].

center of the current sheet can be constructed. Taking the time derivative of the trajectory yields the current sheet speed profile, as illustrated in Fig. 9(b). Similarly, the evolution of the canting angle can be constructed by comparing the anode probe position curve with the cathode probe position at fixed times; Fig. 9(c) shows the results of such an analysis (the canting angle is defined as the angle between a line normal to the cathode and a line tangent to the surface of the current sheet). These data show that current sheet canting is not a continuously evolving phenomenon but, rather, the degree of canting is set up in about the first ten centimeters, after which the current sheet maintains a fairly constant canting angle—in this case, about 60°–70°.

3. Interferometric measurements

A two-chord laser interferometer was implemented to measure the current sheet speed, canting angle and electron density. In addition to the propellants described in the preceding section, methane was tested. The interferometry experiment was carried out in a manner completely analogous to the magnetic field measurement experiment: two axially separated laser beams (configuration 1) were used to measure the current sheet speed and two vertically separated beams (configuration 2) were used to measure the canting angle. Only four spatial locations were probed, all near the midsection of the accelerator and, therefore, do not provide detailed spatial information about the evolution of the electron density.

Figure 10 shows examples of electron density measurements acquired with the interferometer using argon propellant. Figure 10(a) shows a typical result using the interferometer in configuration 1. In this case the laser beams were axially separated by about 11 cm. It is seen that the time delay between the two signals was about 2.5 μs—indicating a propagation speed of about 4.5 cm/μs. Also, this figure indicates that the electron density decreased as the current sheet propagated between the upstream and downstream beams.

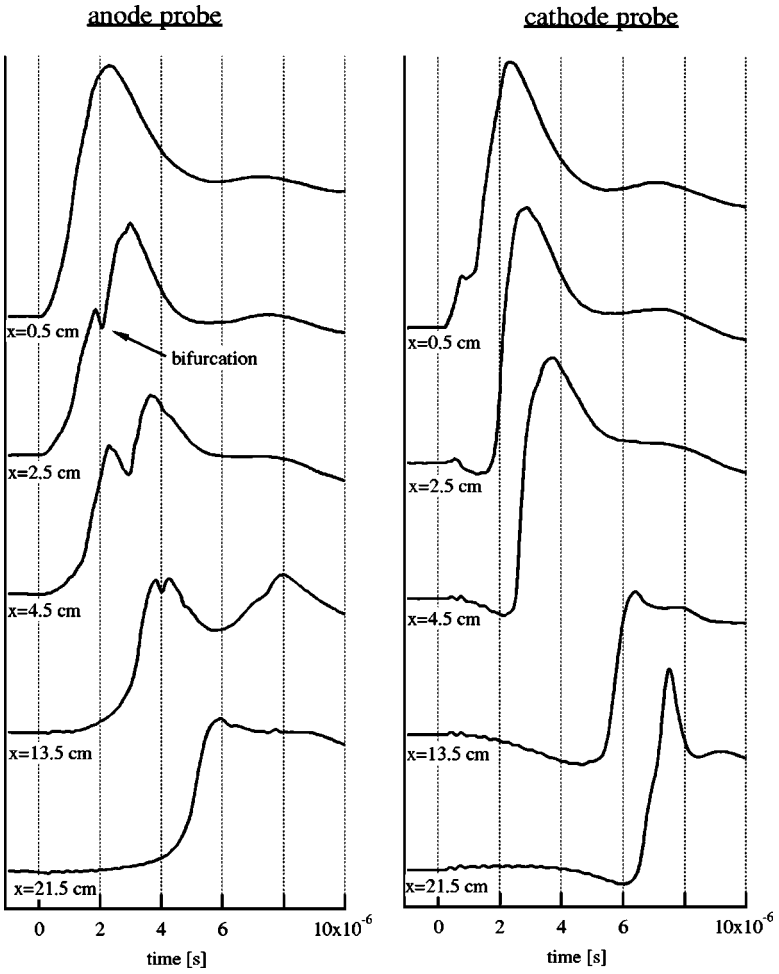

FIG. 8. Magnetic field histories at selected axial locations (argon, $p=75$ mTorr). For reference, the peak value of the magnetic field for both the anode and cathode probes were measured to be about 0.7 T at the $x=0.5$ cm location.

Figure 10(b) shows a typical result using the interferometer in configuration 2 (4 cm vertical beam separation) with the same initial propellant loading as in Fig. 10(a). The anode signal is seen to arrive about 1.5 μs before the cathode signal, in agreement with our previous (magnetic field) observations that the anode current sheet attachment leads the cathode attachment. Multiplying the anode-cathode time delay by 4.5 cm/μs (the sheet propagation speed), yields an axial anode-cathode arc attachment separation of about 7 cm, so that the canting angle may be estimated to be about 60°. Another readily apparent feature in Fig. 10(b) is the large disparity in electron density near the cathode as compared to near the anode, possibly indicating that plasma was being driven toward the cathode by the tilted current sheet. Also, the cathode trace indicates that a layer of plasma persists along the cathode long after the current sheet has passed by as is also seen in the photographs.

Figure 10(c) shows a summary of the peak electron density at the accelerator midsection for all of the propellants tested. The plotted values were compiled from data obtained using the upstream probe in configuration 1. For reference, horizontal lines have been added to indicate the initial (neutral) propellant fill number density for the specified initial pressure levels. The measured electron densities were up to an order of magnitude higher than the initial fill density indicating either local compression of the propellant, or entrainment of propellant in the current sheet.

C. Terminal canting angle

The terminal canting angle was measured near the midsection of the accelerator. As described in the magnetic field mapping section, the canting angle is expected to remain fairly constant throughout this region. Laser interferometry and time-of-flight analysis was used to provide an accurate measurement of the canting angle for each of the propellants.

Figure 11 shows measured canting angle as a function of propellant atomic mass for two pressure levels. When plotting atomic mass, it was assumed that all molecular species were fully decomposed. A mean value of atomic mass was assumed for methane. Each data point is the result of ten experimental measurements; the error bar represents a 90% confidence level. The data in Fig. 11 show that the canting angle rapidly diverges with increasing propellant atomic mass, and then levels off. It is also seen that increased propellant pressure (with hydrogen, deuterium, and methane) resulted in a significantly lower canting angle.

VI. DISCUSSION AND CONCLUSIONS

The current sheet canting experiment has provided new insight into the problem of current sheet canting in pulsed electromagnetic accelerators. Photographic and magnetic field diagnostics show that canting evolves during the early stages of the discharge and is related to bifurcation of the current channel near the anode. Magnetic field measurements

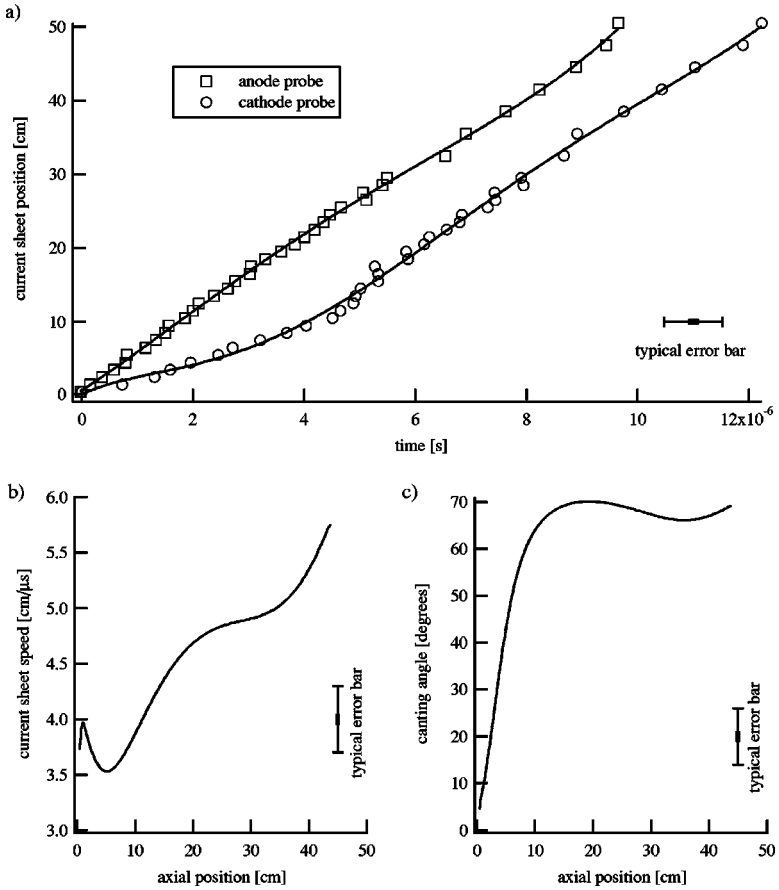

FIG. 9. Evolution of current sheet canting interpreted from magnetic field probe data (argon, 75 mTorr): (a) trajectory of anode and cathode current sheet attachment, (b) current sheet speed as a function of axial position, (c) current sheet canting angle as function of axial position.

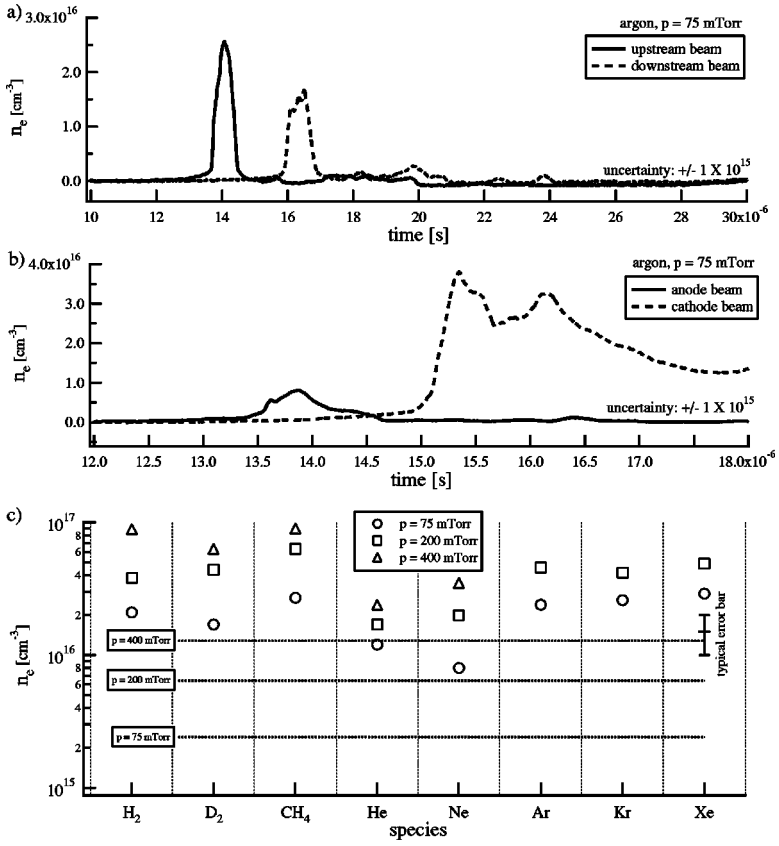

FIG. 10. Example electron density profiles for laser beams aligned in (a) configuration 1 and (b) configuration 2 (argon, $p=75$ mTorr). The peak electron density at the accelerator midsection, for each of the propellants tested, is plotted in (c).

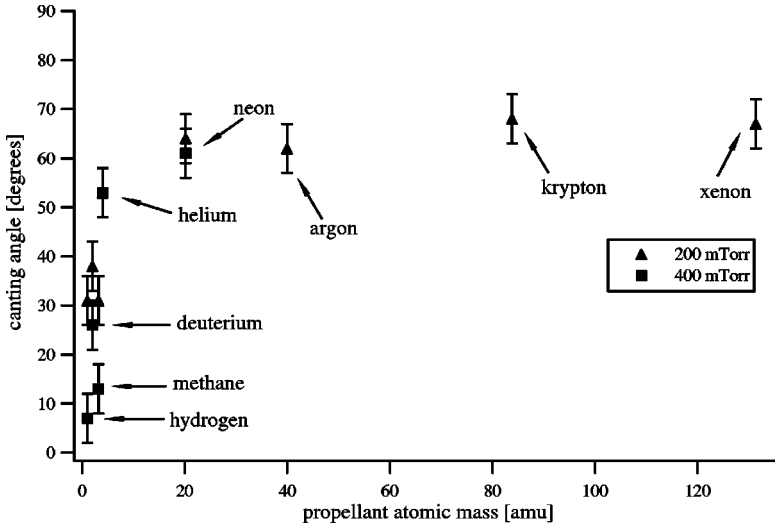

FIG. 11. Terminal canting angle measurements derived from interferometry data, for 200 and 400 mTorr initial pressure levels.

showed that the canting angle stabilizes in the first several microseconds of propagation, and laser-interferometric diagnostics were used to provide quantitative measurements of terminal canting angles. The canting angle was shown to depend on the atomic mass of the propellant; lighter atoms were observed to yield less canting (the measured angles ranged from $\approx 10°$ for hydrogen to 70° for xenon). Molecular propellants which contain hydrogen (hydrogen, deuterium, and methane were tested) showed a pronounced reduction in canting at the highest pressure levels.

The physical mechanism that drives canting is still not fully understood; however, the measurements provided by the present study suggest directions for modeling and, in turn, connecting microscopic phenomena to the macroscopic evolution of a canted current sheet. Clearly, canting is related to near-anode phenomena that occur during the early stages of the discharge. We are presently refining a phenomenological model that attempts to describe the evolution of the current sheet along the anode. In short, it is postulated that a density gradient forms along the anode (directed normal to the anode) with a characteristic length on the order of the ion Larmor radius. The presence of this density gradient allows for rapid penetration of the magnetic field through this region, due to the Hall effect, leading to a canted current front ahead of the initial current conduction channel (this "Hall-convective" form of field transport is described in Ref. 18). Once the current sheet reaches appreciable speeds, entrainment of stationary propellant replenishes plasma in the anode region, inhibiting further Hall-convective transport of the magnetic field, and the current sheet propagates at a relatively constant angle for the remainder of the discharge cycle. Variations in the ion Larmor radius (which affects the characteristic length of the anode density gradient) and ion skin depth, amongst the various propellants, leads to different predicted terminal canting angles. Although more work is required to understand the formation of the near-anode density gradient, using order of magnitude estimates, our phenomenological canting model, which we hope to present in a future paper, captures the general trends of the experimental data—decreased canting with decreasing atomic mass and increasing pressure.

The practical implications of this experimental study are evident. The data show that the most direct way to inhibit current sheet canting is to use low atomic mass propellants at high pressure. In this study hydrogen, deuterium, and methane showed markedly lower canting at higher pressures; however, hydrogen is not an ideal PPT propellant, due to the difficulty of handling cryogenic propellants on a spacecraft. To practically exploit the benefits of reduced current sheet canting that results from the use of hydrogen at high pressure, alkanes, with their hydrogen-rich C_NH_{2N+2} structure, may be a natural choice. Methane was tested as part of the experimental study and was found to have the same reduced canting behavior (at higher pressures) as hydrogen. Further tests are needed on longer-chain hydrocarbons. If butane, for example, is found to exhibit similar behavior, it will be an appealing GFPPT propellant on two levels. In addition to the aforementioned canting benefits, butane can be stored as a liquid under relatively low pressure, at room temperature; therefore, a butane propellant system will have a much smaller specific volume (smaller fuel tank and feed system) than a high pressure gas system, and provide a lower overall system α (mass per unit input power).

ACKNOWLEDGMENTS

The authors gratefully acknowledge the technical assistance provided by Robert Sorenson, and the loan of the Imacon camera from Professor Richard Miles. This research was supported by the Air Force Office of Scientific Research (Grant No. F49620-98-1-0119).

[1] J. Marshall, Phys. Fluids **3**, 134 (1960).
[2] R. Jahn, *Physics of Electric Propulsion*, (McGraw-Hill, New York, 1968).
[3] K. Polzin, E. Choueiri, P. Gurfil, and N. Kasdin, AIAA J. **39**, 347 (2002).
[4] J. Keck, Phys. Fluids **5**, 630 (1962).
[5] F. Fishman and H. Petschek, Phys. Fluids **5**, 632 (1962).
[6] R. Johansson, Phys. Fluids **8**, 866 (1964).
[7] W. Bostick, Phys. Fluids **6**, 1598 (1963).
[8] L. Burkhardt and R. Lovberg, Phys. Fluids **5**, 341 (1962).

[9]L. Liebing, Phys. Fluids **6**, 1035 (1962).
[10]J. MacLelland, A. MacKenzie, and J. Irving, AIAA Research Notes, 1613 (1966).
[11]R. Lovberg, IEEE Trans. Nucl. Sci. **11**, 187 (1964).
[12]R. Burton, Ph.D. thesis, Princeton University, 1966.
[13]T. Markusic, Ph.D. thesis, Princeton University, 2002.
[14]A. Eckbreth, Ph.D. thesis, Princeton University, 1968.
[15]R. Jahn and K. Clark, AIAA J. **4**, 351 (1966).
[16]D. Tilley, A. Gallimore, A. Kelly, and R. Jahn, Rev. Sci. Instrum. **65**, 678 (1994).
[17]J. Huba, NRL Plasma Formulary, Naval Research Laboratory, 1994.
[18]A. Fruchtman, Phys. Fluids B **3**, 1908 (1991).